RESEARCH ARTICLE

Key Points:

- CMAQ-newHg-Br was updated to version 2 with a new gas-particle partitioning (GPP) scheme and the most up-to-date Hg redox chemistry
- CMAQ-newHg-Br v2 better simulated gaseous elemental mercury (GEM), particulate bound mercury (PBM) and Hg wet deposition
- The new GPP scheme captured the observed K_p-T relation not using measurement data and improved nighttime and less polluted simulations

Improving Simulation of Gas-Particle Partitioning of Atmospheric Mercury Using CMAQ-newHg-Br v2

L. Wu[1] [ORCID], H. Mao[1] [ORCID], Z. Ye[2,3], T. S. Dibble[1], A. Saiz-Lopez[4] [ORCID], and Y. Zhang[5] [ORCID]

[1]Department of Chemistry, State University of New York College of Environmental Science and Forestry, Syracuse, NY, USA, [2]Deparment of Environmental Science, Aarhus University, Roskilde, Denmark, [3]iCLIMATE Aarhus University Interdisciplinary Centre for Climate Change, Roskilde, Denmark, [4]Department of Atmospheric Chemistry and Climate, Institute of Physical Chemistry Rocasolano, CSIC, Madrid, Spain, [5]School of Atmospheric Sciences, Nanjing University, Nanjing, China

Abstract Mercury (Hg) is a global pollutant whose atmospheric deposition is a major input to the terrestrial and oceanic ecosystems. Gas-particle partitioning (GPP) of gaseous oxidized mercury (GOM) redistributes speciated Hg between gas and particulate phase and can subsequently alter Hg deposition flux. Most 3-dimensional chemical transport models either neglected the Hg GPP process or parameterized it with measurement data limited in time and space. In this study, CMAQ-newHg-Br (Ye et al., 2018, https://doi.org/10.1002/2017ms001161) was updated to CMAQ-newHg-Br v2 by implementing a new GPP scheme and the most up-to-date Hg redox chemistry and was run for the northeastern United States over January-November 2010. CMAQ-newHg-Br v2 reproduced the measured spatiotemporal distributions of gaseous elemental mercury (GEM) and particulate bound mercury (PBM) concentrations and Hg wet deposition flux within reasonable ranges and simulated dry deposition flux in agreement with previous studies. The GPP scheme improved the simulation of PBM via increasing winter-, spring- and fall-time PBM concentrations by threefold. It also improved simulated Hg wet deposition flux with an increase of 2.1 ± 0.7 μgm^2 in the 11-month accumulated amount, offsetting half of the decreasing effect of the updated chemistry (-4.2 ± 1.8 μgm^2). Further, the GPP scheme captured the observed K_p-T relationship as reported in previous studies without using measurement data and showed advantages at night and in rural/remote areas where existing empirical parameterizations failed. Our study demonstrated CMAQ-newHg-Br v2 a promising assessment tool to quantify impacts of climate change and emission reduction policy on Hg cycling.

Plain Language Summary Mercury is a toxic global pollutant and can enter the food chain through atmospheric deposition to ecosystems. Atmospheric mercury was defined operationally in the forms of gaseous elemental mercury (GEM), gaseous oxidized mercury (GOM) and particulate bound mercury (PBM). GEM is relatively inert, but GOM and PBM are highly soluble and readily removed from the air via deposition. GEM gets oxidized to GOM and GOM can be transformed to PBM through gas particle partitioning (GPP). CMAQ-newHg-Br v2 was updated from its predecessor via implementing the most up-to-date Hg redox chemistry and a new GPP scheme. The model improved the simulation of GEM, PBM, and Hg wet deposition. Most notably the model reproduced the observed partitioning coefficient and temperature relationship (K_p-T) and improved nighttime and less polluted PBM simulations. CMAQ-newHg-Br v2 can be used to assess how climate change and emission reduction policy impact environmental Hg cycling.

1. Introduction

Mercury (Hg) is a global pollutant that cycles and exchanges within and between the atmosphere, terrestrial ecosystems, and aquatic ecosystems (Obrist et al., 2018; Zhang et al., 2009). Atmospheric Hg is operationally defined as gaseous elemental mercury (GEM; Hg(0) in reactions), gaseous oxidized mercury (GOM), and PBM. GEM, with a lifetime of 0.5–1 year, can be oxidized to gaseous oxidized mercury (GOM), which can further be transformed into PBM via gas-particle partitioning (GPP) with relatively short lifetimes ranging from hours to weeks (Schroeder & Munthe, 1998). Reactive mercury (=GOM + PBM) can be removed from the atmosphere through wet and dry deposition, which is one major input for Hg in the oceanic and terrestrial ecosystems. Because of the different chemical and physical characteristics of GEM, GOM and PBM, knowledge of their transformation mechanisms with laboratory-based kinetics supported by ambient measurements is needed to

quantify regional to global budgets of Hg. However, ambient measurements are scarce, which has been one major impediment to the advancement of atmospheric Hg research.

GPP is an important process to the transformation among GEM, GOM and PBM. In general, only the GOM to PBM transformation was considered because Hg(0) has a high vapor pressure of 0.18 Pa at 20°C, which makes its sorption to particles negligible. To simplify the GPP calculation in CTMs, earlier modeling studies treated GOM partitioning as a temperature independent process. For instance, the original CMAQ-Hg model assumes the ratio of PBM:GOM to be 1:1 of the product of Hg + O_3/OH/Cl and the product of Hg + Cl_2/H_2O_2 being entirely GOM (Bullock & Brehme, 2002). Rutter and Schauer (2007) was the first to demonstrate the temperature dependence of reactive mercury partition coefficients (Equations S1 and S2 in Supporting Information S1) through experiments using dry urban aerosols and laboratory generated aerosols from ammonium sulfate and adipic acid mixed with mercuric chloride in a temperature-controlled laboratory reactor. Other studies derived empirical coefficients (K_p) using measured GOM, PBM and particulate matter (PM), and further regressed a K_p-T relationship to quantify the GPP process (Amos et al., 2012; Cheng et al., 2014; Zhang et al., 2019). Note that these field/laboratory measurement-based methods calculated the partition coefficient for measured bulk GOM. Thus, the calculated coefficient could not differentiate individual GOM species and was most likely location- and time period-dependent. Such methods can be a source of uncertainty because of the varying chemical and physical properties of individual GOM species and largely varying environmental conditions as well as uncertainties in GOM and PBM measurements.

Another method often used for GPP calculation is a mass transfer method, originally developed by Schwartz (1986) to deal with two processes involved in mass transfer of gases in clouds: gas phase diffusion to the cloud drop surface and gas-kinetic collisions at the gas-water interface. Jacob (2000) estimated uptake of gases by dry aerosol (i.e., aerosols outside clouds) using Schwartz (1986)'s equation. However, mass transfer is driven by a departure from equilibrium, determined by the partitioning coefficient of a specific chemical species, while adsorption is driven by van der Waals forces and hydrophobic interactions influenced by factors such as the air temperature, enthalpy and vapor pressure of that species, and active sorption sites of the particle surface. For Hg GPP, studies suggested that adsorption via organic bonding sites on aerosol was a dominant pathway (Seigneur et al., 1998). Thus, a mass transfer equation is inadequate in simulating Hg GPP. Yet, Hg modeling studies in the current literature either used empirical formula derived from measurement data or accounted for mass transfer processes only. For example, in simulating PBM, Shah et al. (2021) used the mass-transfer method from Jacob (2000) together with an empirical equilibrium taken from Amos et al. (2012). To match the high upper tropospheric GOM concentration as reported in measurement studies (Gratz et al., 2015; Lyman & Jaffe, 2012), they assumed that the Hg(II) species outgassed from aerosols were all $HgCl_2$ and remained stable against photolysis.

Tekran instruments have been generally deployed to measure GEM, GOM, and PBM at long-term monitoring sites. Tekran PBM measurement data are limited for $PM_{2.5}$, and studies have suggested significant under-biases in Tekran GOM measurements (Gustin et al., 2013; Jaffe et al., 2014; McClure et al., 2014). In addition, a wide range of GOM species have been suggested by computational chemistry studies (Dibble et al., 2012; Goodsite et al., 2012; Jiao & Dibble, 2017; Shah et al., 2021), warranting treatment of speciated GOM. Alternative approaches are thus needed to better represent the GPP process for reactive Hg species in CTMs.

To date, atomic bromine (Br) has been suggested as the dominant oxidant of Hg(0) via a two-step process with HgBr as the intermediate (Goodsite et al., 2004, 2012; Tossell, 2003). Similar reactions were suggested to occur with Cl and OH (Dibble et al., 2020; Donohoue et al., 2005). After the initial Hg(0) oxidation to Hg(I), Hg(I) was further oxidized by O_3, NO_2, HO_2, ClO, BrO to form Hg(II) (Dibble et al., 2012; Gomez Martin et al., 2022; Jiao & Dibble, 2015, 2017; Saiz-Lopez et al., 2020). Photoreduction reactions, which convert gaseous Hg (II) and Hg (I) back to Hg(0), were suggested to play an important role in mercury redox chemistry by Saiz-Lopez et al. (2018, 2019, 2020). A most recent study by Shah et al. (2021) implemented the most comprehensive, at the time, Hg redox chemistry in a global CTM, GEOS-Chem, and obtained a lifetime of 5.5 months for GEM, consistent with observations, and reproduced observed Hg wet deposition fluxes. They suggested Br and OH being comparable Hg(0) oxidants and O_3 being the principal Hg(I) oxidant. Recently more experimental and computational studies have been published, such as the first experimental reaction rate constants of HgBr + O_3/NO/O_2 by Gomez Martin et al. (2022), Wu et al. (2022), Lam, Wilhelmsen, and Dibble (2019), Lam, Wilhelmsen, Schwid's, et al. (2019) BrHgO + RH• reaction and Khiri et al. (2020)'s BrHgO + CO reaction, the last two could be crucial BrHgO sinks.

Table 1
Simulation Cases

Case	Gas-phase chemistry	GPP
Y2018	CMAQ-newHg-Br v1	No
BASE	CMAQ-newHg-Br v1 + 38 photoreduction +35 new redox reactions	Yes
NoGPP	CMAQ-newHg-Br v1 + 38 photoreduction +35 new redox reactions	No

New reactions and kinetic data need to be added and updated for Hg chemical mechanisms in 3-D CTMs to better capture atmospheric redox chemistry.

In this study, we developed a new GPP scheme, which calculated the partition coefficients for individual GOM species based on theoretical prediction of both adsorption and absorption (Pankow, 1994). We implemented the new GPP scheme in a modified CMAQ-Hg, namely, CMAQ-newHg-Br v2, which was updated from our previous version, CMAQ-newHg-Br (Ye et al., 2018), by adding new Hg redox reactions and updating kinetic data. CMAQ-newHg-Br v2 was evaluated against measurement data of GEM and PBM as well as Hg wet deposition flux from the National Atmospheric Deposition Program (NADP, https://nadp.slh.wisc.edu/). Three model simulation cases were conducted for January-November 2010 over the northeastern US to quantify the impacts of the new GPP scheme together with the updated chemistry.

2. Methods

2.1. Model Description and Configuration

For this study, CMAQ v5.3.2 was set up in a Lambert Conformal domain over the northeastern United States with spatial resolution of 12 km × 12 km horizontal grids and 35 vertical layers and was run for the period of January 15th–November 30th 2010 with a 15-day spin-up. Note that we originally aimed to simulate four complete seasons. However, the winter season of 2010 had to be reduced to 1.5 months due to the limited availability of meteorological model simulation and the global chemical transport model, GEOS-Chem output, the latter of which was used as initial and boundary conditions for our regional simulations. Nonetheless, our simulations did illustrate our modified model's improved capability in cold month simulations as shown in Section 3. The domain and resolution are identical to Ye et al. (2018). Briefly, CMAQ-newHg-Br v2 was driven by meteorological fields simulated using the Weather Research and Forecast (WRF) model (Michalakes et al., 2004; Skamarock et al., 2008) and were provided by the Atmospheric Chemistry and Aerosol Branch, Atmospheric & Environmental Systems Modeling Division, Center for Environmental Measurement and Modeling of the US EPA. The monthly averaged concentrations from a three-dimensional global chemistry model GEOS-Chem (Y. Zhang, Jaegle, et al., 2012) were used as the initial and boundary conditions for our simulations as done in Ye et al. (2018). The EPA National Emission Inventory (NEI) 2011 were used to prepare emission input using the Sparse Matrix Operator Kernel Emissions model (Houyoux et al., 2000). The speciation of Hg emissions was referenced in the 2005 version 4.1 platform (https://www.epa.gov/air-emissions-modeling/2005-version-41-platform) based on 2005 NEI version 2.

The model was compiled with the multipollutant version of Carbon-Bond version 6 (CB6) chemical mechanism (Yarwood et al., 2010), which includes updated halogen chemistry, an online photolysis, and the multipollutant AERO6 aerosol module. Details on updated gas-phase Hg chemistry were provided in Section 2.2. A cloud module with Hg sorption to cloud droplets was used (Pleijel & Munthe, 1995). Hg aqueous chemistry, including photoreduction of organic Hg^{2+} compounds with dicarboxylic acids (Bash et al., 2014; Si & Ariya, 2008) was used. The new air-surface exchange model, Surface Tiled Aerosol and Gaseous Exchange (STAGE) (Appel et al., 2021) was used to calculate gas and aerosol dry deposition, as well as GEM bidirectional exchanges (Appel et al., 2021). STAGE unifies the bidirectional and unidirectional deposition schemes using the resistance model frameworks of Massad et al. (2010) and Nemitz et al. (2001). A brief description of STAGE can be found in Section 3 in the Supporting Information S1. A detailed description of the Hg bidirectional model can be found in Bash (2010).

Three simulation cases were designed as shown in Table 1. The BASE case, using the complete modified model CMAQ-newHg-Br v2, included the most up-to-date Hg redox chemistry with a new GPP scheme. The Y2018

case used our previously developed Hg-Br chemical mechanism from CMAQ-newHg-Br v1 (Ye et al., 2018). The NoGPP case included the most up-to-date Hg redox chemistry without the new GPP scheme. Hence the difference between the BASE and NoGPP cases quantified the effects of our new GPP scheme, and that between the Y2018 and the NoGPP cases quantified the effects of our most up-to-date Hg redox chemistry.

2.2. Hg Gas Phase Chemistry

The Hg-Br chemical mechanism in CMAQ-newHg-Br v1 included 20 gas-phase Hg reactions and a detailed Br chemical mechanism (Ye et al., 2018). In this study, we updated that mechanism by adding 35 Hg redox reactions and 38 photoreduction reactions. Tables S1 and S2 in Supporting Information S1 showed all the 55 gas-phase reactions and 38 photoreduction reactions. Three major updates to the Hg chemistry mechanism in CMAQ-newHg-Br v2 were summarized below.

First, HgO was removed as a product of $Hg(0) + O_3$ and $Hg(0) + OH$ reactions since studies showed that gas phase HgO was endoergic and unlikely to exist in gas phase (Calvert & Lindberg, 2005; Shepler & Peterson, 2003; Subir et al., 2011). O_3 was no longer employed as an oxidant to initiate $Hg(0)$ oxidation, instead, as a second step oxidant to react with HgBr, HgCl and HgOH to form $Hg(II)$ (Castro et al., 2022; Gomez Martin et al., 2022; Saiz-Lopez et al., 2020). The first experimental rate constants measured by Gomez Martin et al. (2022) reported as $(7.5 \pm 0.6) \times 10^{11} cm^3$ molecules$^1(1\sigma)$ was used in this study. $Hg(0) + OH$ was implemented as one of the $Hg(0)$ oxidation reactions to form HgOH and was further oxidized by OH, HO_2, NO_2, ClO to form $Hg(II)$ as described above and the rate constant was from Dibble et al. (2020), Jiao and Dibble (2017), Wu et al. (2020).

Second, gas-phase $Hg(I)$ and $Hg(II)$ reduction reactions were added. NO_2, NO and CO were added as $Hg(I)$ and $Hg(II)$ reductants (Khiri et al., 2020; Wu et al., 2020, 2022).

Third, rate constants were updated and new HgBr/HgBrO reactions added. The rate constant of $HgBr + NO_2$ was updated based on the recent experimental work conducted by Wu et al. (2020), and the same rate constant was used for $HgCl/HgOH + NO_2$. For the $HgBr + HO_2$ reaction, the rate constant calculated by Jiao and Dibble (2017) was used. A new HgBr reaction $HgBr + O_2$ was added based on Wu et al. (2022)'s most recent experimental work. A series of hydrogen abstraction reactions of $HgBrO + CH_4/HCHO$ and the $HgBrO + C_2H_4$ reaction, which may change the speciation of GOM, were added based on computational work of Lam, Wilhelmsen, and Dibble (2019), Lam, Wilhelmsen, Schwid's, et al. (2019).

2.3. Gas-Particle Partitioning

The original CMAQ-Hg model (Bullock & Brehme, 2002) did not include GOM GPP for dry aerosols, but only accounted for chemical partitioning for cloud droplets. Of all the 5 GEM oxidation reactions included, it was assumed that half of the products of $Hg + O_3$, $Hg + Cl$ and $Hg + OH$ went to solid phase, which was how PBM was obtained through secondary pathways in CMAQ-Hg (Bullock & Brehme, 2002). According to the experimental study conducted by Jones et al. (2016), Ye et al. (2018) assumed, in CMAQ-newHg-Br v1, that the products of $Hg + O_3/OH$ reactions deposited to the Earth's surface in the first layer and were transformed to PBM in the second layer and above.

In this study, instead of using empirical partitioning coefficients as reviewed in Introduction, a theoretical equation (Pankow, 1994) was used to quantify GPP of individual GOM species to PBM. Equation 1 below calculated both the adsorptive and absorptive contributions to the coefficient for GOM compound i (GOM_i), $K_{p,i}$ (m^3/μg):

$$K_{p,i} = \frac{1}{p_{L,i}^\circ}\left[\frac{N_s a_{\text{tsp}} T e^{\frac{Q_1 - Q_v}{RT}}}{1600} + \frac{f_{\text{PBM}} 760 RT}{MW_{\text{PBM}} \zeta_i 10^6}\right] \tag{1}$$

The first term of Equation 1 calculates adsorption and the second absorption. In Equation 1, R is the gas constant (8.314 Pa m^3 K^1 mol^1 in the first term and 8.206×10^5 m^3 atmK^{-1} mol^{-1} in the second term), T is air temperature (K), $p_{L,i}^\circ$ is the vapor pressure (torr) of GOM_i as a liquid at T, N_s is the surface concentration of sorption sites (mol cm^{-2}), which corresponds to the surface concentration of organic aerosols (OA), a_{tsp} is the specific surface area for the TSP (m^2 g^{-1}), Q_1 (KJ mol^{-1}) is the enthalpy of desorption of compound i from the adsorbing, solid
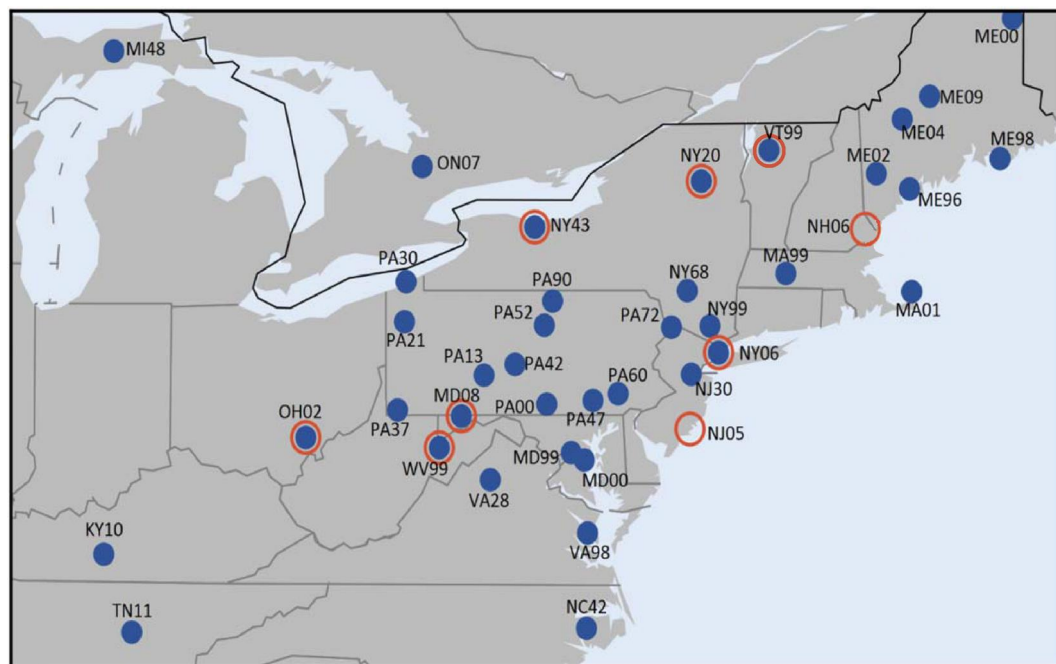
Figure 1. Locations of 38 MDN sites (blue dots) and 9 AMNet sites (red circles).

surface, and Q_v (KJ mol^{-1}) is the enthalpy of vapourization of compound i as a liquid. For absorbing material, f_{PBM} is the weight fraction of the *TSP* that comprise the absorbing aerosols, which was assumed to be OA (Seigneur et al., 1998). Both N_s and f_{PBM} were computed using model simulated variables. MW_{PBM} is the molecular weight of PBM$_i$ (g mol^{-1}), and ζ_i is the activity coefficient. An activity coefficient of 1 was used (Schell et al., 2001).

At the present time, vapor pressure values are available for HgBr$_2$, HgCl$_2$ and HgI$_2$ only (Stull, 1947). In this study, the lowest vapor pressure value of the three, that is, that of HgI$_2$, was applied to all other GOM species. The lower the vapor pressure, the larger the GPP effect. We conducted tests using the three existing vapor pressure values and compared simulated PBM concentrations with measured data. The results indicated that the HgI$_2$ vapor pressure value allowed simulated PBM concentrations in closest agreement with measurements and hence it was applied in the model. In addition, due to the lack of experimental and ambient data, the $\frac{Q_1-Q_v}{R}$ constant, a value of 10, was estimated by forcing the seasonal cycle of PBM concentrations calculated using the variables from the NoGPP case to agree with the observed from all the AMNet sites within the model domain. Considering that it was derived for all the 26 GOM species under a great range of atmospheric physical and chemical conditions from the hourly output of a 11-month simulation over domain-wide locations, the estimated $\frac{Q_1-Q_v}{R}$ constant was thus probably the best approximation at the present time. This constant can be replaced as soon as experimental values of Q_1 and Q_v of individual GOM species become available in the future.

2.4. Model Evaluation

Simulated ambient Hg concentrations were evaluated using available observational data of the nine sites in the northeastern US (Figure 1) from the Atmospheric Mercury Network (AMNet; http://nadp.sws.uiuc.edu/ amn/). The accuracy of measurements has significant influence on model evaluation and hence development. Here, our modified model was evaluated using GEM and PBM measurement data only due to the large uncertainty of Tekran GOM measurements (Cheng & Zhang, 2017; Jaffe et al., 2014). GEM and PBM concentrations were measured using Tekran 2537 and 1135 with detection limits of 0.01 ng m^{-3} and 1.0 pg m^{-3}, respectively (Gay et al., 2013; Mao et al., 2012; Sigler et al., 2009). Units of observed GEM were converted to ppqv and 2 hr average data were used for model evaluation. PBM measurements were only for PM$_{2.5}$ (Gustin et al., 2019), and hence we evaluated the simulated PBM for PM$_{2.5}$ only.

Table 2
Model Evaluation Metrics for Comparing the BASE, NoGPP, and Y2018 Simulations With Measurements of Gaseous Elemental Mercury and Particulate Bound Mercury at 9 AMNet Monitoring Sites Within the Modeling Domain

	Obs	BASE	Y2018	NoGPP
GEM				
Mean (ppqv)	171.6	157.1	152.6	157.7
MB (ppqv)		−14.5	−19.5	−14.3
NMB (%)		−8.3	−11.0	−7.9
NME (ppqv)		0.17	0.18	0.16
FB (%)		−9.0	−11.9	−8.6
PBM				
Mean (pg m^{-3})	8.0	18.4	5.3	5.4
MB (pg m^{-3})		11.0	0.12	0.07
NMB (%)		186.6	−12.3	−11.6
NME (pg m^{-3})		2.4	0.9	1.0
FB (%)		52.8	−35.7	−35.4

Weekly accumulated Hg wet deposition flux measurement data from the 38 Mercury Deposition Network (MDN; http://nadp.sws.uiuc.edu/MDN/) sites in the domain (Figure 1) were used for model evaluation. Simulated hourly Hg wet deposition flux data were summed to weekly data for comparison with observations. Hg dry deposition flux was compared with available data from previous measurement and modeling studies.

Six metrics were used for model evaluation: mean value, mean bias (MB), fractional bias (FB), mean error (ME), normalized mean bias (NMB), and normalized mean error (NME) defined as Equations S3–S7 in Supporting Information S1.

3. Results and Discussion

3.1. Model Evaluation

3.1.1. Evaluation of Ambient Concentration Simulations

Model evaluation metrics were calculated using simulated GEM and PBM concentrations and observational data from 9 AMNet sites within the domain during January 15th–November 30th 2010 (Table 2) and compared with other CMAQ-Hg studies. The BASE and NoGPP cases had higher mean GEM concentrations of 157 ppqv both with smaller MB, ∼−14 ppqv, NMB, −8% and FB, ∼−9% than the Y2018 case did. The BASE case showed simulated GEM concentrations closer to observations with NMB of −8% and NME of 0.17, compared to the underestimates with NMB of −23% and NME of 0.25 from Bieser et al. (2016). Note that Bieser et al. (2016) used the original CMAQ-Hg model with five GEM oxidation reactions (Hg + O$_3$, H$_2$O$_2$, Cl$_2$, OH and Cl). The BASE case overestimated PBM with 187% NMB, 11 pg m^{-3} MB, and 52% FB while our Y2018 and NoGPP cases expectedly underestimated PBM, with ∼−12% NMB, ∼−12 pg m^{-3} MB, and −36% FB.

Simulated GOM concentrations were not evaluated in this study due to uncertainties in the Tekran GOM measurements. However, the magnitude of simulated GOM concentrations was put into perspective via comparison with AMNet observations. The BASE case showed an average of 0.68 ppqv GOM versus the observed 0.48 ppqv. Gustin et al. (2013) showed that concentrations of reactive Hg (RM) measured using their new method were two- to three-fold higher than those measured by the Tekran system, which indicated that our simulated GOM was underestimated.

The seemingly larger deviation from observed PBM concentrations shown in the BASE case simulation was likely attributed to the uncertainties in the parameters in Equation 1. For instance, due to the lack of experimental and measurement parameters for GOM species, as pointed out in the Methods section, the $\frac{Q_1 - Q_v}{R}$ constant was derived from forcing the seasonal cycle of PBM concentrations calculated using NoGPP output to agree with the observed. In addition, the uniform application of the constant to all GOM species was a simplification that most likely did not reflect the diverse nature of the wide range of GOM species. Simulated PBM concentrations are anticipated to improve with the availability of experimental or ambient measurement-based values for the Q_1 and Q_v parameters for all GOM species.

All the three cases exhibited similar seasonal patterns with higher GEM in the winter, spring, and fall and lower in the summer, which was consistent with observations (Figure 2a), but overestimated seasonal amplitude (=annual maximum—minimum). Cases BASE and NoGPP performed better than Y2018 with monthly mean GEM concentrations showing 5–6 ppqv higher in all four seasons, closer to the observed values. Observed ground-level PBM concentrations showed higher concentrations in January–March with a range of 1–35 pg m^{-3}, and lower concentrations in the summer, 0−18 pg m^{-3}, and fall, 0−16 pg m^{-3} (Figure 2b). In addition, simulated seasonal amplitude was 428 pg/m^3, 205 pg/m^3 and 185 pg/m^3 for the BASE, NoGPP and Y2018 case, respectively, compared to that of 385 pg/m^3 from the AMNet measurement data. The BASE case exhibited the highest concentrations of PBM in January, averaging 11.7 pg/m^3, agreeing in both magnitude and timing with the AMNet data displaying an annual maximum of 11.8 pg/m^3 in January, whereas the NoGPP and Y2018 cases showed
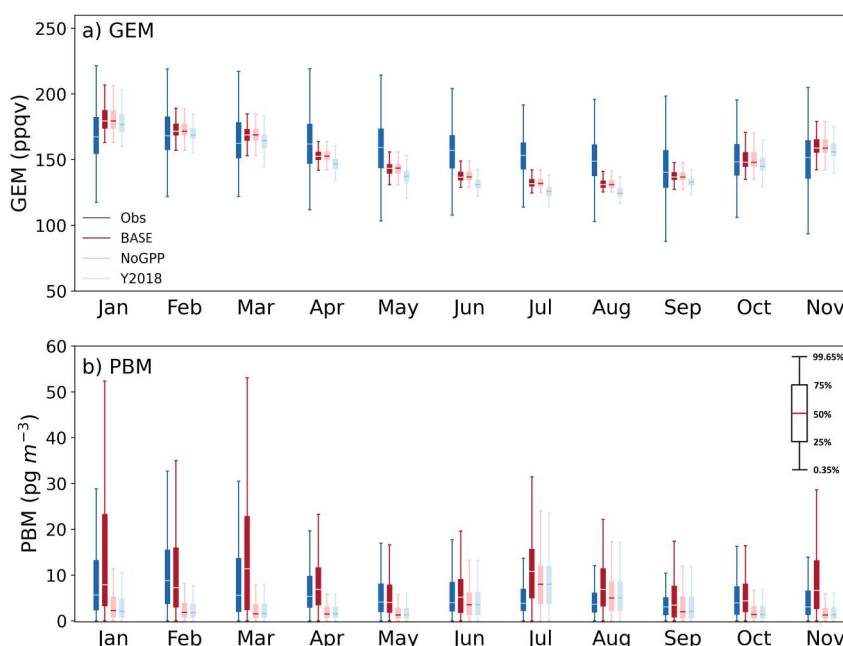
Figure 2. Seasonal variations in observed (dark blue) and modeled (BASE in maroon, NoGPP in pink, and Y2018 in light blue) hourly (a) gaseous elemental mercury and (b) particulate bound mercury.

annual maximums of 7.7 pg/m^3 in July. It was apparent that of all the three cases, the seasonal amplitude and pattern simulated in the BASE case were in the closest agreement with the AMNet observations (Figure 2b).

The summertime overestimation of PBM in the BASE case probably resulted from uncertainties in the parameters used as aforementioned, as well as overestimated PBM emissions (Holloway et al., 2012; Lin et al., 2006) and underpredicted surface air temperature, especially in the summer months, and overpredicted RH (Yahya et al., 2016), the latter two of which enhanced the GPP effect. The improved seasonal simulation was mainly attributed to the new GPP scheme via increasing winter-, spring- and fall-time PBM concentrations by threefold.

A closer examination revealed that the BASE case simulated PBM concentrations at rural sites, with mean value of 7 pg m^{-3} and FB of 33%, better than at urban/suburban sites, with mean value of 28 pg m^{-3} and FB of 103%. This contrast may be ascribed to an average of 2.5°C lower temperature at the rural sites resulting in more secondary PBM captured by the GPP scheme than at the urban/suburban sites. Unlike PBM, GEM was better simulated by the BASE case at urban and suburban sites, with mean GEM of 171 ppqv and −1% FB, than at the rural sites, with mean GEM of 150 ppqv and −15% FB. As GEM was influenced predominantly by emission sources, the spatial distribution of GEM was consistent with the distribution of GEM anthropogenic emissions as shown in Figure S1 in Supporting Information S1.

Vertical distributions of Hg species have been of great interest and remain elusive, which is one aspect that is difficult to be reproduced by models (Mao et al., 2016; Shah et al., 2021; Ye et al., 2018). All the three cases (Figure S2 in Supporting Information S1) showed similar vertical distributions, where GOM concentrations increased with altitude, from <1 ppqv at the ground level to >7 ppqv near the tropopause, similar to the simulation results of GEOS-Chem from Shah et al. (2021). Studies attributed large GOM concentrations at high altitudes to more abundant Br radicals, lack of depositional loss, and lower temperature (Brooks et al., 2014; Gratz et al., 2015; Lyman & Jaffe, 2012; Shah et al., 2016; Sillman et al., 2007). Aircraft measurements showed an average of 15 ppq HgII in the free troposphere in northern midlatitudes (Saiz-Lopez et al., 2020). Shah et al. (2016) simulated hundreds of pg m^{-3} GOM in the upper troposphere using GEOS-Chem. However, Shah et al. (2021), using the same model with updated Hg redox chemistry, were unable to reproduce those values. Our Y2018 case simulated the highest 11-month mean GOM concentration at 27 ppqv, averaged from altitudes above 10 km at noontime (Figure S2 in Supporting Information S1), whereas the NoGPP case, with the most up-to-date chemistry, simulated about a factor of 3 lower GOM concentrations of ∼10 ppqv. With the new GPP scheme in the BASE case, simulated GOM was further reduced to ∼7 ppqv. GEM of all the three cases showed similar
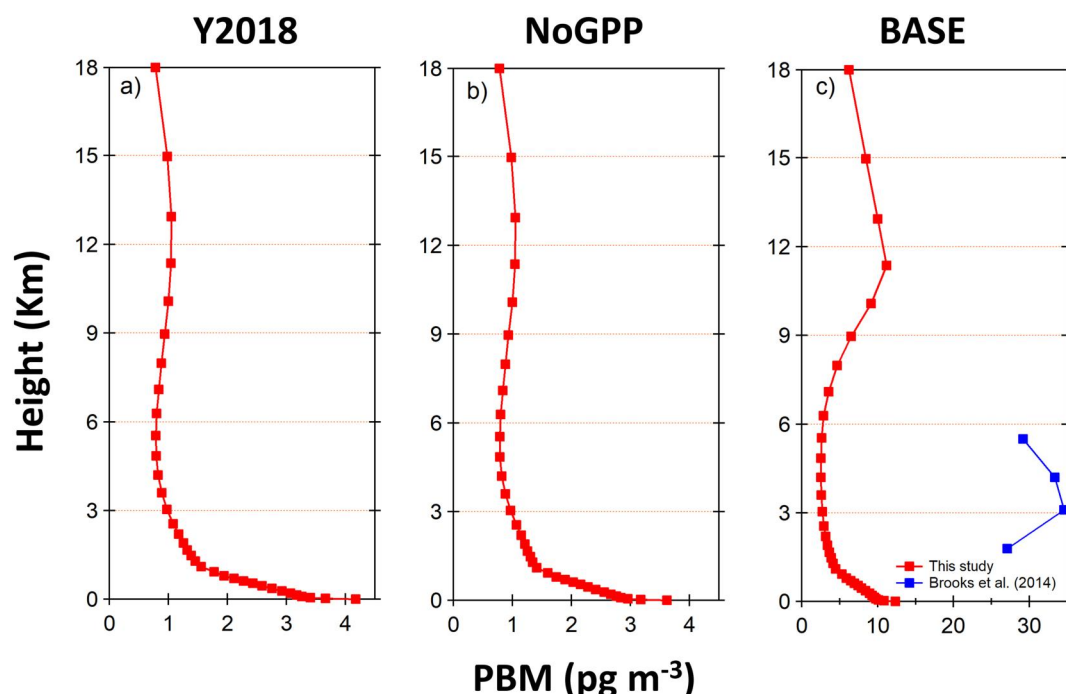
Figure 3. Averaged vertical profiles of particulate bound mercury of all 9 AMNet sites at noontime from the Y2018, NoGPP and BASE cases. The vertical profile in blue was adapted from Brooks et al. (2014).

vertical profiles with the highest GEM near the ground level and decreased with increasing height, while the observations of Brooks et al. (2014) showed relatively constant GEM concentrations near the ground. The BASE and NoGPP cases showed higher GEM than Y2018 at all heights (Figure S2 in Supporting Information S1). For PBM, all our three cases did not experience the peak at 3–4.5 km shown in Brooks et al. (2014)'s 7-month averaged measurements conducted in Tullahoma, TN, which is outside of our modeling domain (Figure 3).

3.1.2. Evaluation of Simulated Wet and Dry Deposition Fluxes

Our simulated wet deposition flux was evaluated using weekly observations from the 38 MDN sites in the domain (Table 3). The evaluation metrics of the three cases suggested reasonable model-observation agreement compared to previous studies (Baker & Bash, 2012; Bieser et al., 2014; Bullock et al., 2009; Horowitz et al., 2017; H. Zhang,

Table 3
Evaluation Metrics for Simulated Weekly Hg Wet Deposition Flux in the BASE, NoGPP, and Y2018 Cases, Compared With Measurement Data at the 38 MDN Sites in the Domain

Reference	Region	MB	FB (%)	ME	NMB (%)	NME	R^2
BASE (This study)	NE US	−34	−21	−21	−19	−0.1	0.27
NoGPP (This study)	NE US	−80	−58	−66	−45	−0.4	0.25
Y2018 (This study)	NE US	24	13	37	14	0.2	0.25
Bullock et al. (2009)	North America	−12		178	−5	0.70	0.15
Baker and Bash (2012)	EUS	−171–61	−45–35	121–253			
Baker and Bash (2012)	WUS	210–467	51–110	295–513			
Bieser et al. (2014)	Europe	−30		36			0.91
H. Zhang, Holmes, and Wu (2016)	North America	−5					0.26
Horowitz et al. (2017)	North America						0.32
Zhang and Zhang (2022)	North America						0.64

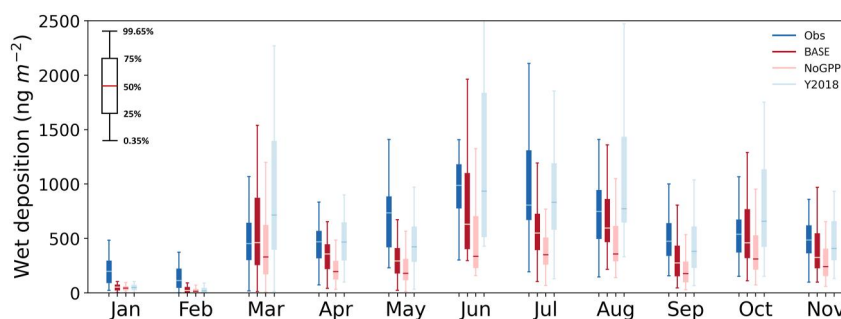*Note.* NE US represents the Northeast US, EUS the East US, and WUS the west US.

Figure 4. Seasonal variations in observed and simulated monthly accumulated Hg wet deposition flux during January–November 2010 at 38 MDN sites in the domain.

Wu, et al., 2016; Zhang & Zhang, 2022). The BASE and Y2018 cases showed better simulation results, with smaller values of MB, FB, ME, NMB and NME, for wet deposition compared with the NoGPP case (Table 3). The comparison revealed underestimates of 19% and 5% in the BASE and NoGPP cases, respectively, and an overestimate of 14% in the Y2018 case. Our BASE case simulated wet deposition flux, 3–15 μg m^{-2}, was in the similar range as that in Shah et al. (2021), 2–12 μg m^{-2}, for the northeastern US. The underestimation in the BASE and NoGPP cases was caused mainly by the newly added photoreduction reactions, which decreased GOM concentrations by 34%, causing a 50% decrease in GOM wet deposition flux on average. To compare, the new GPP scheme decreased GOM by 25% and increased PBM by 231% on average, resulting in a net increase of 52% in Hg wet deposition flux.

Seasonal variations in wet deposition flux were reproduced by all the three cases with larger values in the spring and summer than in the fall and winter. Our results showed that BASE case outperformed the NoGPP case in all four seasons (Figure 4) and has a slightly better R^2 of 0.27 compared with observations than the other two cases (Table 3). All three cases exhibited the highest total wet deposition in summer, agreed with observations. The seasonal amplitude for all three cases were 2.0 μg/m^2, 1.3 μg/m^2, and 3.0 μg/m^2 for the BASE, NoGPP, and Y2018 cases, respectively. In comparison, observations showed an amplitude of 2.6 μg/m^2. While Y2018-simulated seasonal amplitude appeared to be closest to the observed, the BASE case outperformed the NoGPP case. The BASE case underestimated Hg wet deposition flux in the spring, summer and fall by 16%, 16% and 11%, respectively, while the Y2018 case overestimated by 18%, 31% and 22%. All three cases underestimated Hg wet deposition flux in winter by ∼70%. The wintertime underestimation was also shown in Selin and Jacob (2008) using GEOS-Chem. Two factors may contribute to the underestimated GOM. First, winter-time precipitation was underpredicted by 34% compared to observations. Second, the average concentration of GOM simulated in the BASE case was only 0.38 ppqv, significantly lower than the observed value of 0.60 ppq, the latter of which was already a factor of two to three under-biased as indicated by Gustin et al. (2019).

Due to the lack of observational data, our estimates of annual Hg dry deposition flux were compared with previous studies (Table 4). Our 11-month totals were scaled to 12 months for comparison. L. Zhang, Blanchard, et al. (2012); L. Zhang, Wu, et al. (2016) calculated annual Hg dry deposition flux with dry deposition velocities simulated using the Big-leaf model combined with measured Hg concentrations. Our simulated annual amounts were 7.8–20.0, 8.9–33.0, and 13–83.3 μgm^{-2} in the BASE, NoGPP, and Y2018 cases, respectively, in reasonable agreement with the range of 5.2–26.1 μgm^{-2} during 2008–2009 from L. Zhang, Blanchard, et al. (2012) and 3.1 − 18.7 μgm^{-2} over 2009 − 2014 from H. Zhang, Wu, et al. (2016). Of all the three cases, the BASE case simulated the lowest 11-month total Hg dry deposition, ∼37% less than the highest amount in the Y2018 case, resulting from a significant decrease in GOM, ∼50%, owing to the added photoreduction reactions and GPP scheme.

3.2. Effects of Gas-Particle Partitioning

3.2.1. Effects on Speciated Mercury

The effect of the GPP scheme was quantified from the difference between the BASE and NoGPP cases, with Δ = BASE–NoGPP and Δ in % = (BASE–NoGPP)/NoGPP ×100%. The GPP scheme significantly decreased GOM by up to 93%, that is, −20 ppqv (Figure 5a) and increased PBM by up to 1,915%, that is, 365 pg m^{-3} (Figure 5b). A marked seasonal pattern was found with, on average, larger increases and decreases in PBM and

Table 4

Simulated Accumulated Hg dry Deposition ($\mu g m^{-2}$) During January–November 2010 in the Three Cases and Compared With Estimations From H. Zhang, Wu, et al. (2016); L. Zhang, Blanchard, et al. (2012), and Litterfall Measurements From Risch et al. (2017)

	This study					
Site	BASE	NoGPP	Y2018	H. Zhang, Wu, et al. (2016)	L. Zhang, Blanchard, et al. (2012)	Risch et al. (2017)
MD08	10.0	11.0	18.7	10.5	14.9	15.3 ± 2.1
NH06	9.8	10.7	18.0	7.7	21.2	
NJ05	9.4	11.0	19.6	18.7	26.1	
NY06	20.0	33.0	83.3	8.0	9.2	
NY20	8.7	9.3	14.0	10.8	5.2	11.2 ± 0.6
NY43	7.8	9.0	13.8	8.5	13.8	
OH02	8.3	8.9	13.1	4.5	13.3	18.8 ± 2.8
VT99	9.5	10.2	16.1	9.0	12.7	11.3 ± 1.8
WV99	12.4	13.7	22.6	3.1	12.2	9.3 ± 1.0

GOM, respectively, in the winter, spring, and fall than in the summer (Figure 5b). The seasonality was mainly driven by temperature, causing a higher tendency for GOM to be partitioned to solid phase in the colder months of the winter, spring and fall. GEM concentrations hardly varied (Figure S5 in Supporting Information S1).

As reviewed in Introduction, current studies either parameterized GPP with measurement data or used Schwartz (1986)'s mass transfer equation, which do not fully represent the GPP process. Our new GPP scheme included both adsorption and absorption, and their relative importance was examined here to support our point. Detailed analysis suggested that the inclusion of adsorption only, absorption only, or both was able to produce the observed PBM seasonal pattern (Figure 6a). However, the magnitude was best simulated with adsorption and absorption both included, especially in the spring and fall. The seasonal pattern of ΔPBM (Figure 6b) resulted from the effect of meteorological conditions, PM and OA concentrations, of which OA provided efficient bonding sites for GOM as reviewed in Sections 1 and 2. Three salient features were shown in the seasonal variation in the effect of GPP on PBM. First, ΔPBM showed an opposite seasonal pattern compared to that of temperature, higher in winter, spring and fall whereas lower in the summer, in agreement with previous studies (Amos et al., 2012; Rutter & Schauer, 2007). Second, OA concentrations were 13% higher in the spring than in the fall, hence
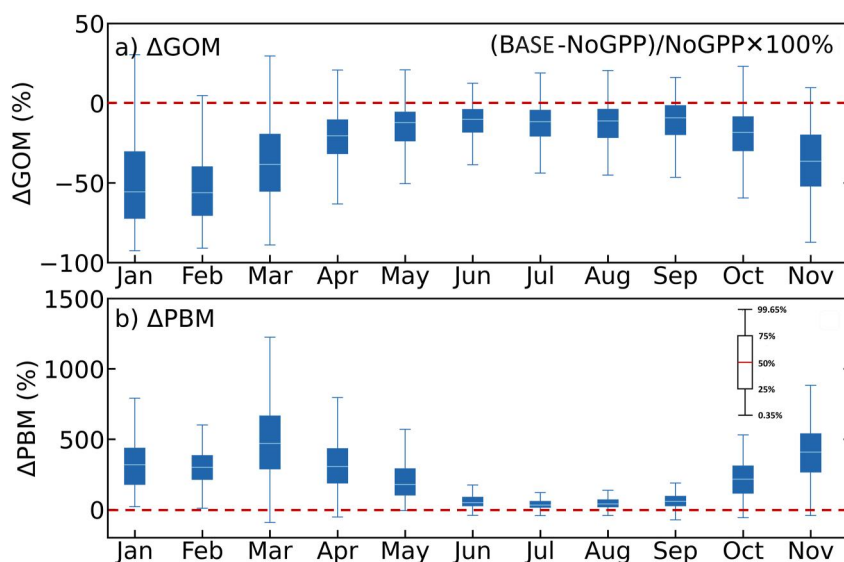

Figure 5. GPP-induced changes in surface (a) gaseous oxidized mercury and (b) particulate bound mercury concentrations at the 9 AMNet sites in the model domain.
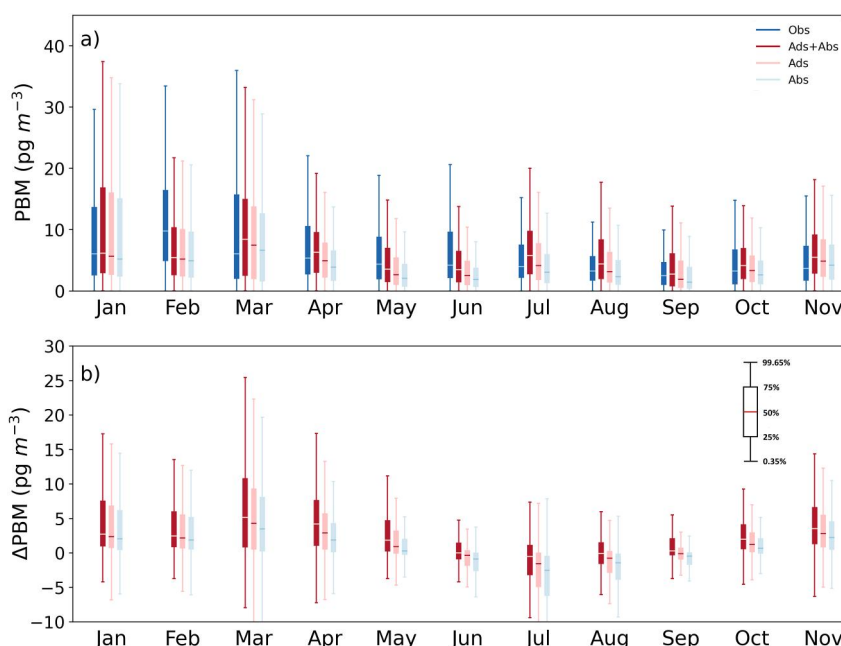
Figure 6. Seasonal variations in panel (a) particulate bound mercury concentrations with adsorption, absorption, and adsorption plus absorption against observations, and (b) the corresponding ΔPBM values compared to the NoGPP case.

providing more bonding sites resulting in larger ΔPBM. Third, the highest GPP in the spring was attributed to the highest relative humidity in March 2010, which led to unusually high water uptake by PM conducive to larger surface areas for adsorption (Cheng et al., 2014). Additionally, March was one of the colder months (Figure S6 in Supporting Information S1) but with higher OA concentrations, 30% higher than the average of the other spring months and fall months (Figure S6 in Supporting Information S1) and saw the second highest GOM concentrations with a monthly average of 0.41 ppqv of the BASE case (Figure S3 in Supporting Information S1).

To compare our results with the existing measurement-based parameterizations in the literature as reviewed in Section 1, a relationship between the partition coefficient (K_p) and air temperature (T) was shown as follows (Figure 7):

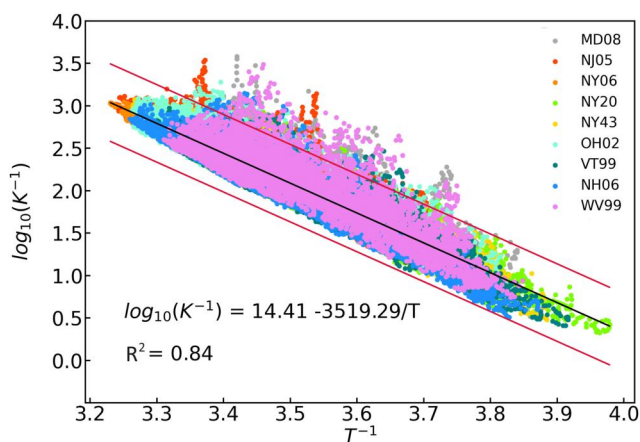$$\log_{10} K_p^{-1} = 14.41 - 3519.29/T \qquad (2)$$

Figure 7. Simulated temperature dependence of the partition coefficient (K_p). The black line represents the linear regression, while the two red lines indicate the one standard deviation range. Each distinct color corresponds to one of the nine observation sites.

using modeled results from the 9 AMNet site locations. Our K_p-T correlation showed the highest R^2 value, 0.84, larger than that of Rutter and Schauer (2007), and the slope and intercept values were within the ranges reported by Amos et al. (2012), Rutter and Schauer (2007), Cheng et al. (2014), and Liu et al. (2022) (Table 5). Note that our K_p-T relationship was derived from the model simulation employing Equation 1, whereas the K_p-T relationships in those three studies were derived based on field measurement data from at best a handful of monitoring locations. The comparison (Table 5) suggested that our theory-based approach captured the observed K_p-T relationships without the need of measurement data. Further, we identified outliers as the data points exceeding one standard deviation from the fitted line (Figure 7). Most of the outliers turned out to correspond to relatively low mean PM levels of 2.7 μg m^{-3}, mean GOM of 0.2 ppqv and PBM of 3.0 pg m^{-3} concentrations, and 70% of the outliers occurred at nighttime, defined here as 7 p.m.–7 a.m. local time. This result indicated that the empirical formula from previous studies could also be limited for rural to remote areas most often with lower PM, GOM and PBM concentrations.

Table 5
Regression Coefficients for $\log_{10}(K_p^{-1}) = a + b/T$

a	b	R^2	Reference
14.41	−3519.29	0.84	This study
10 ± 1	−2,500 ± 300	0.49	Amos et al. (2012)
15 ± 2	−4,250 ± 480	0.77	Rutter and Schauer (2007)
7 ± 1	−1,710 ± 380	0.49	Rutter and Schauer (2007)
12.69	−3485.30	0.55	Cheng et al. (2014)
10 ± 1	−2,700 ± 280	0.45	Liu et al. (2022)
8 ± 1	−2,100 ± 230	0.31	Liu et al. (2022)

Averaged noontime vertical distributions of ΔGEM, ΔGOM, and ΔPBM in percentage (Figure 8) showed that the decreasing effect of our new GPP scheme on GEM concentrations was negligible. The GPP scheme did not change GEM concentrations directly but through changing GOM concentrations. Specifically, the more GOM was transformed to PBM, the less GOM was available for photoreduction back to GEM. Overall, GPP decreased GOM concentrations at all altitudes with two largest decreases, −50% to −40% captured at the ground level and ∼10 km altitude. The maximum positive effect of the GPP scheme on PBM concentrations was observed at 11.4 km altitude with an increase of 975% (Figure 8c).

3.2.2. Effects on Hg Deposition

Effects of GPP on monthly accumulated Hg wet deposition fluxes at 38 MDN sites and dry deposition fluxes at 9 AMNet sites were quantified in the domain (Figure 9). GPP increased monthly accumulated Hg wet deposition flux by 52%, offsetting the decreasing effect of −46% from the updated chemistry. As discussed in Section 3.2.1, GPP decreased GOM, increased PBM, and hardly changed GEM concentrations, leading to a GOM wet deposition change of −66%–175%, and PBM wet deposition flux change of 12%–2096%. The overall effect of GPP on Hg wet deposition flux was dominated by an increase of 1,167 ng m⁻², that is, 335%, in wet deposition flux of PBM. The composition of Hg wet deposition changed from GOM and PBM comprising 86% and 13%, respectively, of total wet deposition flux in the NoGPP case to 38% and 62% in the BASE case. The decreases (increases) in GOM (PBM) wet deposition flux caused by the GPP scheme were larger in the spring and fall than in the summer (Figure 8a). As a result, stronger effects on the total (GOM + PBM) wet deposition flux were simulated in the spring, −37%–270%, than in the fall, −62%–164%, and summer, −29%–131%. However, the winter season did not show the largest Hg wet deposition change, which probably due to underpredicted snow amounts and GOM concentrations, as discussed in Section 3.1.2 Model Evaluation. While no distinct seasonal patterns were shown for changes in GOM and total Hg dry deposition flux, PBM dry deposition was increased by 385%, 248%, 221%, and 51% in the spring, winter, fall, and summer, respectively, in accordance with the seasonal patterns of ΔPBM determined with the GPP scheme.
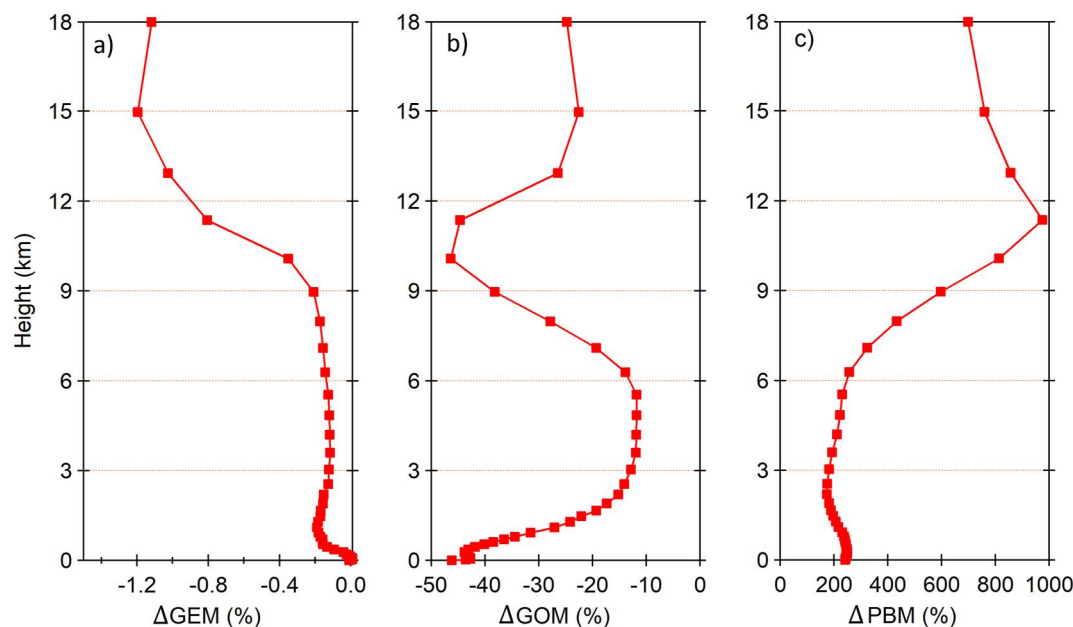

Figure 8. Modeled vertical profiles of percent changes in panel (a) gaseous elemental mercury, (b) gaseous oxidized mercury, and (c) particulate bound mercury concentrations caused by the new gas-particle partitioning scheme. Δ% = (BASE−NoGPP)/NoGPP × 100%
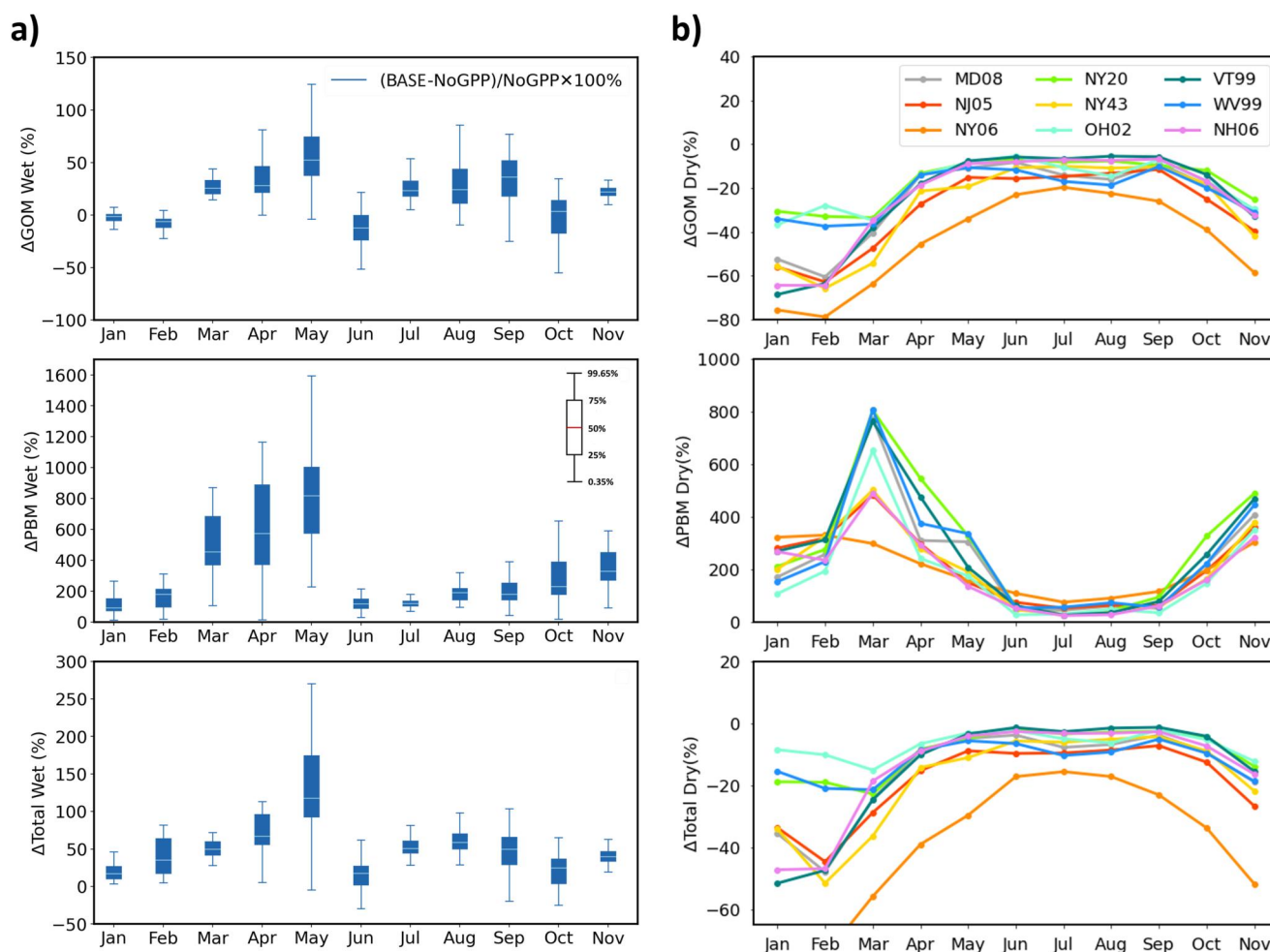
Figure 9. Percentage changes, caused by the gas-particle partitioning scheme, in modeled monthly accumulated gaseous oxidized mercury, particulate bound mercury, and total (a) wet deposition flux at the 38 MDN sites and (b) dry deposition flux at the 9 AMNet sites.

3.3. GPP Versus Updated Chemistry

To put the effects of the new GPP scheme in perspective, the effects of the updated chemistry on Hg species as well as Hg wet and dry deposition fluxes were quantified. The effects of the updated chemistry were the difference between the NoGPP and Y2018 simulations, denoted as Δ = NoGPP–Y2018; Δ in % = (NoGPP–Y2018)/Y2018 (Table 6). On average, while GPP decreased GOM by 25%, 0.47 ppqv and increased PBM concentrations by 231%, 10.8 pg m^{-3}, the updated chemistry increased GEM by 4%, 5.2 ppqv, decreased GOM by 34%, 0.41 ppqv. Different from that of GPP, the effect of the updated chemistry was larger in the summer than in the spring and fall (Figure S7 in Supporting Information S1). The updated chemistry had overall decreasing effects on Hg wet and dry deposition fluxes, while GPP decreased Hg dry deposition flux but increased Hg wet deposition flux. On average, the GPP scheme increased the 11-month accumulated wet deposition flux by 2.1 ($\pm$0.7) μgm^{-2}, half the decreasing effect of the updated chemistry by −4.2 ($\pm$1.8) μgm^{-2}. The GPP scheme had comparable decreasing effects, which is −2.1 ($\pm$4.0) μgm^{-2} on dry deposition flux as the updated chemistry did, −3.5 ($\pm$1.7) μgm^{-2}.

Vertically, the decreasing effect of the updated chemistry on GOM strengthened with increasing altitude and peaked in the upper troposphere (Figure S8 in Supporting Information S1), a pattern similar to that of GPP, but its magnitude, which was −66% to −42% was significantly stronger than that of GPP, −46% to −11%. Saiz-Lopez et al. (2018)'s calculations showed that most Hg(II) absorbed UV-VIS of 160–220 nm, which should happen more readily at higher altitudes with stronger radiation fluxes at such wavelengths. The updated chemistry changed the magnitude of GEM and GOM concentrations at all altitudes without changing the vertical pattern compared to the Y2018 case.

Table 6
Site-Averaged Changes in Gaseous Elemental Mercury, Gaseous Oxidized Mercury, and Particulate Bound Mercury Concentrations, and 11-Month Accumulated Dry and Wet Deposition Changes Caused by Gas-Particle partitioning, Defined as BASE − NoGPP and Updated Chemistry, Defined as NoGPP–Y2018

	GPP		Updated chemistry	
	Absolute	Percentage	Absolute	Percentage
Speciated Hg				
ΔGEM (*ppqv*)	−2–10	−1%–1%	0–18	0%–15%
ΔGOM (*ppqv*)	−15–0.3	−97%–62%	−3.3–0	−78%–7%
ΔPBM (pgm^{-3})	−5–257	−92%–1,750%	−0.3–0.2	−15%–10%
Deposition (μgm^{-2})				
ΔDry Deposition	−13.3 to −0.3	−56% to −6%	−6.3 to −0.8	−38% to −17%
ΔWet Deposition	1.1–3.7	26%–66%	−11.4 to −1.8	−61% to −38%

All the three cases showed similar vertical distributions while only the Y2018 case was able to capture the high free tropospheric GOM concentration of 15 ppqv averaged from aircraft measurements (Saiz-Lopez et al., 2020; Sillman et al., 2007) (Figure S2 in Supporting Information S1), as shown in Section 3.1.1 Model Evaluation. All the three cases simulated the highest GOM concentrations at the tropopause (Figure S2 in Supporting Information S1). As for GEM, the vertical profiles from the aircraft measurements were captured near the surface by all the three cases, the highest concentrations simulated by NoGPP, with a larger decreasing trend as altitude increase.

4. Summary

In this study, a theory-based GPP scheme was developed and, together with the most up-to-date mercury redox chemistry, implemented in CMAQ-newHg-Br v2. Model evaluation against NADP measurement data demonstrated that CMAQ-newHg-Br v2 was able to simulate observed spatiotemporal variations in GEM and PBM concentrations as well as Hg wet deposition flux within reasonable ranges. Simulated dry deposition flux was in close agreement with previous studies. Overall, GPP decreased surface GOM concentrations by $25 \pm 23\%, 0.47 \pm 1.54$ ppqv and increased PBM by $231 \pm 240\%, 10.9 \pm 28.8$ pg m^{-3} while the updated chemistry decreased GOM by $34 \pm 14\%, 0.41 \pm 0.38$ ppqv with slight effects on GEM $3.6 \pm 2\%, 5.1 \pm 2.8$ ppqv and PBM $1.4 \pm 6.7\%, 0.04 \pm 0.6$ pg m^{-3}. The new GPP scheme improved the simulation of PBM seasonal variations and captured a significant fraction of secondary PBM while the updated chemistry improved the simulation of GEM. The new GPP scheme better captured the observed K_p-T relationship than the existing methods in the literature likely for rural to remote areas and nighttime periods. Of all the three cases, the BASE case performed the best in simulating Hg wet deposition flux owing to the new GPP scheme. The effect of GPP on Hg concentrations and depositions was strong in the winter, spring and fall while the updated chemistry in the summer. Together these two could have significant impacts on Hg cycling throughout the simulation period. It should be noted that the underestimation of GOM concentrations as well as Hg wet deposition flux indicated insufficient GOM production and missing GEM oxidation pathways. The initial and boundary conditions from the global model GEOS-Chem could induce uncertainties because of inconsistencies between the two different models. Moreover, there remained large uncertainties in the kinetics data used; a large fraction of the reactions and rate constant were from computational calculations with no support from in-situ measurement or lab experiment data. However, this modified model demonstrated a promising capability to better quantify atmospheric mercury sources and sinks and will be useful to assessments of the efficacy of anthropogenic emission control and the impact of climate change on atmospheric Hg cycling, which is an important component of the Minamata Convention.

Data Availability Statement

The CMAQ-5.3.2 source code used for simulation is freely available at https://www.cmascenter.org/cmaq/. The observational ambient Hg data used for model evaluation in the study are available at the AMNet website via https://nadp.slh.wisc.edu/networks/atmospheric-mercury-network/. The observational Hg wet deposition data

used for model evaluation in the study are available at the MDN website via https://nadp.slh.wisc.edu/networks/mercury-deposition-network/.

The code of the Gas-Particle Partitioning module and the model simulation data are publicly available at https://github.com/lwu127/GPP (Wu, 2024).

References

Amos, H. M., Jacob, D. J., Holmes, C. D., Fisher, J. A., Wang, Q., Yantosca, R. M., et al. (2012). Gas-particle partitioning of atmospheric Hg(II) and its effect on global mercury deposition. *Atmospheric Chemistry and Physics*, *12*(1), 591–603. https://doi.org/10.5194/acp-12-591-2012

Appel, K. W., Bash, J. O., Fahey, K. M., Foley, K. M., Gilliam, R. C., Hogrefe, C., et al. (2021). The Community Multiscale Air Quality (CMAQ) model versions 5.3 and 5.3.1: System updates and evaluation [Article]. *Geoscientific Model Development*, *14*(5), 2867–2897. https://doi.org/10.5194/gmd-14-2867-2021

Baker, K. R., & Bash, J. O. (2012). Regional scale photochemical model evaluation of total mercury wet deposition and speciated ambient mercury. *Atmospheric Environment*, *49*, 151–162. https://doi.org/10.1016/j.atmosenv.2011.12.006

Bash, J. O. (2010). Description and initial simulation of a dynamic bidirectional air-surface exchange model for mercury in Community Multiscale Air Quality (CMAQ) model [Article]. *Journal of Geophysical Research*, *115*(15). Article D06305. https://doi.org/10.1029/2009jd012834

Bash, J. O., Carlton, A. G., Hutzell, W. T., & Bullock, O. R. (2014). Regional air quality model application of the aqueous-phase photo reduction of atmospheric oxidized mercury by dicarboxylic acids [Article]. *Atmosphere*, *5*(1), 1–15. https://doi.org/10.3390/atmos5010001

Bieser, J., De Simone, F., Gencarelli, C., Geyer, B., Hedgecock, I., Matthias, V., et al. (2014). A diagnostic evaluation of modeled mercury wet depositions in Europe using atmospheric speciated high-resolution observations. *Environmental Science Pollution Research*, *21*(16), 9995–-10012. https://doi.org/10.1007/s11356-014-2863-2

Bieser, J., Schrum, C., Blum, J. D., & Soerensen, A. (2016). Impact of marine mercury cycling on coastal atmospheric mercury concentrations in the North- and Baltic Sea region. *Elementa: Science of the Anthropocene*, *4*. https://doi.org/10.12952/journal.elementa.000111

Brooks, S., Ren, X., Cohen, M., Luke, W., Kelley, P., Artz, R., et al. (2014). Airborne vertical profiling of mercury speciation near Tullahoma, TN, USA. *Atmosphere*, *5*(3), 557–574. https://doi.org/10.3390/atmos5030557

Bullock, O. R., & Brehme, K. A. (2002). Atmospheric mercury simulation using the CMAQ model: Formulation description and analysis of wet deposition results. *Atmospheric Environment*, *36*(13), 2135–2146. https://doi.org/10.1016/S1352-2310(02)00220-0

Bullock, O. R., Jr., Atkinson, D., Braverman, T., Civerolo, K., Dastoor, A., Davignon, D., et al. (2009). An analysis of simulated wet deposition of mercury from the North American Mercury Model Intercomparison Study. *Journal of Geophysical Research*, *114*(D8). Article D08301. https://doi.org/10.1029/2008jd011224

Calvert, J. G., & Lindberg, S. E. (2005). Mechanisms of mercury removal by O-3 and OH in the atmosphere. *Atmospheric Environment*, *39*(18), 3355–3367. https://doi.org/10.1016/j.atmosenv.2005.01.055

Castro, P. J., Kello, V., Cernusak, I., & Dibble, T. S. (2022). Together, not separately, OH and O(3) oxidize Hg((0)) to Hg((II)) in the atmosphere. *The Journal of Physical Chemistry A*, *126*(44), 8266–8279. https://doi.org/10.1021/acs.jpca.2c04364

Cheng, I., & Zhang, L. (2017). Uncertainty assessment of gaseous oxidized mercury measurements collected by atmospheric mercury network. *Environmental Science & Technology*, *51*(2), 855–862. https://doi.org/10.1021/acs.est.6b04926

Cheng, I., Zhang, L. M., & Blanchard, P. (2014). Regression modeling of gas-particle partitioning of atmospheric oxidized mercury from temperature data [Article]. *Journal of Geophysical Research-Atmospheres*, *119*(20), 11864–11876. https://doi.org/10.1002/2014jd022336

Dibble, T. S., Tetu, H. L., Jiao, Y. G., Thackray, C. P., & Jacob, D. J. (2020). Modeling the OH-initiated oxidation of mercury in the global atmosphere without violating physical laws [Article]. *Journal of Physical Chemistry A*, *124*(2), 444–453. https://doi.org/10.1021/acs.jpca.9b10121

Dibble, T. S., Zelie, M. J., & Mao, H. (2012). Thermodynamics of reactions of ClHg and BrHg radicals with atmospherically abundant free radicals. *Atmospheric Chemistry and Physics*, *12*(21), 10271–10279. https://doi.org/10.5194/acp-12-10271-2012

Donohoue, D. L., Bauer, D., & Hynes, A. J. (2005). Temperature and pressure dependent rate coefficients for the reaction of Hg with Cl and the reaction of Cl with Cl: A pulsed laser photolysis-pulsed laser induced fluorescence study [Article]. *Journal of Physical Chemistry A*, *109*(34), 7732–7741. https://doi.org/10.1021/jp051354l

Gay, D. A., Schmeltz, D., Prestbo, E., Olson, M., Sharac, T., & Tordon, R. (2013). The atmospheric mercury network: Measurement and initial examination of an ongoing atmospheric mercury record across North America. *Atmospheric Chemistry and Physics*, *13*(22), 11339–11349. https://doi.org/10.5194/acp-13-11339-2013

Gomez Martin, J. C., Lewis, T. R., Douglas, K. M., Blitz, M. A., Saiz-Lopez, A., & Plane, J. M. C. (2022). The reaction between HgBr and O3: Kinetic study and atmospheric implications. *Physical Chemistry Chemical Physics*, *24*(20), 12419–12432. https://doi.org/10.1039/d2cp00754a

Goodsite, M. E., Plane, J. M. C., & Skov, H. (2004). A theoretical study of the oxidation of Hg0 to HgBr2 in the troposphere. *Environmental Science & Technology*, *38*(6), 1772–1776. https://doi.org/10.1021/es034680s

Goodsite, M. E., Plane, J. M. C., & Skov, H. (2012). A theoretical study of the oxidation of Hg0 to HgBr2 in the troposphere (vol 38, pg 1772, 2004) [Correction]. *Environmental Science & Technology*, *46*(9), 5262. https://doi.org/10.1021/es301201c

Gratz, L. E., Ambrose, J. L., Jaffe, D. A., Shah, V., Jaegle, L., Stutz, J., et al. (2015). Oxidation of mercury by bromine in the subtropical Pacific free troposphere. *Geophysical Research Letters*, *42*(23), 10494–10502. https://doi.org/10.1002/2015gl066645

Gustin, M. S., Dunham-Cheatham, S. M., & Zhang, L. (2019). Comparison of 4 methods for measurement of reactive, gaseous oxidized, and particulate bound mercury. *Environmental Science & Technology*, *53*(24), 14489–14495. https://doi.org/10.1021/acs.est.9b04648

Gustin, M. S., Huang, J., Miller, M. B., Peterson, C., Jaffe, D. A., Ambrose, J., et al. (2013). Do we understand what the mercury speciation instruments are actually measuring? Results of RAMIX. *Environmental Science & Technology*, *47*(13), 7295–7306. https://doi.org/10.1021/es3039104

Holloway, T., Voigt, C., Morton, J., Spak, S. N., Rutter, A. P., & Schauer, J. J. (2012). An assessment of atmospheric mercury in the Community Multiscale Air Quality (CMAQ) model at an urban site and a rural site in the Great Lakes Region of North America. *Atmospheric Chemistry and Physics*, *12*(15), 7117–7133. https://doi.org/10.5194/acp-12-7117-2012

Horowitz, H. M., Jacob, D. J., Zhang, Y., Dibble, T. S., Slemr, F., Amos, H. M., et al. (2017). A new mechanism for atmospheric mercury redox chemistry: Implications for the global mercury budget. *Atmospheric Chemistry and Physics*, *17*(10), 6353–6371. https://doi.org/10.5194/acp-17-6353-2017

Houyoux, M. R., Vukovich, J. M., Coats, C. J., Wheeler, N. J. M., & Kasibhatla, P. S. (2000). Emission inventory development and processing for the seasonal model for regional air quality (SMRAQ) project. *Journal of Geophysical Research*, *105*(D7), 9079–9090. https://doi.org/10.1029/1999jd900975

Jacob, D. J. (2000). Heterogeneous chemistry and tropospheric ozone. *Atmospheric Environment*, *34*(12–14), 2131–2159. https://doi.org/10.1016/s1352-2310(99)00462-8

Jaffe, D. A., Lyman, S., Amos, H. M., Gustin, M. S., Huang, J., Selin, N. E., et al. (2014). Progress on understanding atmospheric mercury hampered by uncertain measurements. *Environmental Science Technology*, *48*(13), 7204–7206. https://doi.org/10.1021/es5026432

Jiao, Y., & Dibble, T. S. (2015). Quality structures, vibrational frequencies, and thermochemistry of the products of reaction of BrHg(*) with NO₂, HO₂, ClO, BrO, and IO. *The Journal of Physical Chemistry A*, *119*(42), 10502–10510. https://doi.org/10.1021/acs.jpca.5b04889

Jiao, Y., & Dibble, T. S. (2017). First kinetic study of the atmospherically important reactions BrHg + NO2 and BrHg + HOO. *Physical Chemistry Chemical Physics*, *19*(3), 1826–1838. https://doi.org/10.1039/c6cp06276h

Jones, C. P., Lyman, S. N., Jaffe, D. A., Allen, T., & O'Neil, T. L. (2016). Detection and quantification of gas-phase oxidized mercury compounds by GC/MS. *Atmospheric Measurement Techniques*, *9*(5), 2195–2205. https://doi.org/10.5194/amt-9-2195-2016

Khiri, D., Louis, F., Černušák, I., & Dibble, T. S. (2020). BrHgO● + CO: Analogue of OH + CO and reduction path for Hg(II) in the atmosphere. *ACS Earth and Space Chemistry*, *4*(10), 1777–1784. https://doi.org/10.1021/acsearthspacechem.0c00171

Lam, K. T., Wilhelmsen, C. J., & Dibble, T. S. (2019). BrHgO(*) + C2H4 and BrHgO(*) + HCHO in atmospheric oxidation of mercury: Determining rate constants of reactions with prereactive complexes and bifurcation. *The Journal of Physical Chemistry A*, *123*(28), 6045–6055. https://doi.org/10.1021/acs.jpca.9b05120

Lam, K. T., Wilhelmsen, C. J., Schwid, A. C., Jiao, Y., & Dibble, T. S. (2019). Computational study on the photolysis of BrHgONO and the reactions of BrHgO(*) with CH(4), C(2)H(6), NO, and NO(2): Implications for formation of Hg(II) compounds in the atmosphere. *The Journal of Physical Chemistry A*, *123*(8), 1637–1647.

Lin, C.-J., Pongprueksa, P., Lindberg, S. E., Pehkonen, S. O., Byun, D., & Jang, C. (2006). Scientific uncertainties in atmospheric mercury models I: Model science evaluation. *Atmospheric Environment*, *40*(16), 2911–2928. https://doi.org/10.1016/j.atmosenv.2006.01.009

Liu, K., Wu, Q., Wang, S., Chang, X., Tang, Y., Wang, L., et al. (2022). Improved atmospheric mercury simulation using updated gas-particle partition and organic aerosol concentrations. *Journal of Environmental Sciences*, *119*, 106–118. https://doi.org/10.1016/j.jes.2022.04.007

Lyman, S. N., & Jaffe, D. A. (2012). Formation and fate of oxidized mercury in the upper troposphere and lower stratosphere. *Nature Geoscience*, *5*(2), 114–117. https://doi.org/10.1038/ngeo1353

Mao, H., Cheng, I., & Zhang, L. (2016). Current understanding of the driving mechanisms for spatiotemporal variations of atmospheric speciated mercury: A review. *Atmospheric Chemistry and Physics*, *16*(20), 12897–12924. https://doi.org/10.5194/acp-16-12897-2016

Mao, H., Talbot, R., Hegarty, J., & Koermer, J. (2012). Speciated mercury at marine, coastal, and inland sites in New England - Part 2: Relationships with atmospheric physical parameters. *Atmospheric Chemistry and Physics*, *12*(9), 4181–4206. https://doi.org/10.5194/acp-12-4181-2012

Massad, R. S., Nemitz, E., & Sutton, M. A. (2010). Review and parameterisation of bi-directional ammonia exchange between vegetation and the atmosphere. *Atmospheric Chemistry and Physics*, *10*(21), 10359–10386. https://doi.org/10.5194/acp-10-10359-2010

McClure, C. D., Jaffe, D. A., & Edgerton, E. S. (2014). Evaluation of the KCl denuder method for gaseous oxidized mercury using HgBr2 at an in-service AMNet site. *Environmental Science & Technology*, *48*(19), 11437–11444. https://doi.org/10.1021/es502545k

Michalakes, J., Dudhia, J., Henderson, T., & Klemp, J. (2004). The weather research and Forecast model: Software architecture and performance. In *Proceedings of the 11th ECMWF workshop*.

Nemitz, E., Milford, C., & Sutton, M. A. (2001). A two-layer canopy compensation point model for describing bi-directional biosphere-atmosphere exchange of ammonia. *Quarterly Journal of the Royal Meteorological Society*, *127*(573), 815–833. https://doi.org/10.1256/smsqj.57305

Obrist, D., Kirk, J. L., Zhang, L., Sunderland, E. M., Jiskra, M., & Selin, N. E. (2018). A review of global environmental mercury processes in response to human and natural perturbations: Changes of emissions, climate, and land use. *Ambio*, *47*(2), 116–140. https://doi.org/10.1007/s13280-017-1004-9

Pankow, J. F. (1994). An absorption-model of the gas aerosol partitioning involved in the formation of secondary organic aerosol [Article]. *Atmospheric Environment*, *28*(2), 189–193. https://doi.org/10.1016/1352-2310(94)90094-9

Pleijel, K., & Munthe, J. (1995). Modelling the atmospheric mercury cycle-chemistry in fog droplets. *Atmospheric Environment*, *29*(12), 1441–1457. https://doi.org/10.1016/1352-2310(94)00323-D

Risch, M. R., DeWild, J. F., Gay, D. A., Zhang, L., Boyer, E. W., & Krabbenhoft, D. P. (2017). Atmospheric mercury deposition to forests in the eastern USA. *Environmental Pollution*, *228*, 8–18. https://doi.org/10.1016/j.envpol.2017.05.004

Rutter, A. P., & Schauer, J. J. (2007). The effect of temperature on the gas-particle partitioning of reactive mercury in atmospheric aerosols [Article]. *Atmospheric Environment*, *41*(38), 8647–8657. https://doi.org/10.1016/j.atmosenv.2007.07.024

Saiz-Lopez, A., Acuña, A. U., Trabelsi, T., Carmona-García, J., Dávalos, J. Z., Rivero, D., et al . (2019). Gas-Phase Photolysis of Hg(I) Radical Species: A New Atmospheric Mercury Reduction Process. *Journal of the American Chemical Society*, *141*(22), 8698–8702. https://doi.org/10.1021/jacs.9b02890

Saiz-Lopez, A., Sitkiewicz, S. P., Roca-Sanjuan, D., Oliva-Enrich, J. M., Davalos, J. Z., Notario, R., et al. (2018). Photoreduction of gaseous oxidized mercury changes global atmospheric mercury speciation, transport and deposition. *Nature Communication*, *9*(1), 4796. https://doi.org/10.1038/s41467-018-07075-3

Saiz-Lopez, A., Travnikov, O., Sonke, J. E., Thackray, C. P., Jacob, D. J., Carmona-Garcia, J., et al. (2020). Photochemistry of oxidized Hg(I) and Hg(II) species suggests missing mercury oxidation in the troposphere [Article]. *Proceedings of the National Academy of Sciences of the United States of America*, *117*(49), 30949–30956. https://doi.org/10.1073/pnas.1922486117

Schell, B., Ackermann, I. J., Hass, H., Binkowski, F. S., & Ebel, A. (2001). Modeling the formation of secondary organic aerosol within a comprehensive air quality model system. *Journal of Geophysical Research*, *106*(D22), 28275–28293. https://doi.org/10.1029/2001jd000384

Schroeder, W. H., & Munthe, J. (1998). Atmospheric mercury—An overview. *Atmospheric Environment*, *32*(5), 809–822. https://doi.org/10.1016/S1352-2310(97)00293-8

Schwartz, S. E. (1986). Mass-transport considerations pertinent to aqueous phase reactions of gases in liquid-water clouds. In *Chemistry of multiphase atmospheric systems* (pp. 415–471). https://doi.org/10.1007/978-3-642-70627-1_16

Seigneur, C., Abeck, H., Chia, G., Reinhard, M., Bloom, N. S., Prestbo, E., & Saxena, P. (1998). Mercury adsorption to elemental carbon (soot) particles and atmospheric particulate matter. *Atmospheric Environment*, *32*(14–15), 2649–2657. https://doi.org/10.1016/S1352-2310(97)00415-9

Selin, N. E., & Jacob, D. J. (2008). Seasonal and spatial patterns of mercury wet deposition in the United States: Constraints on the contribution from North American anthropogenic sources. *Atmospheric Environment*, *42*(21), 5193–5204. https://doi.org/10.1016/j.atmosenv.2008.02.069

Shah, V., Jacob, D. J., Thackray, C. P., Wang, X., Sunderland, E. M., Dibble, T. S., et al. (2021). Improved mechanistic model of the atmospheric redox chemistry of mercury. *Environmental Science & Technology*, *55*(21), 14445–14456. https://doi.org/10.1021/acs.est.1c03160

Shah, V., Jaeglé, L., Gratz, L. E., Ambrose, J. L., Jaffe, D. A., Selin, N. E., et al. (2016). Origin of oxidized mercury in the summertime free troposphere over the southeastern US. *Atmospheric Chemistry and Physics*, *16*(3), 1511–1530. https://doi.org/10.5194/acp-16-1511-2016

Shepler, B. C., & Peterson, K. A. (2003). Mercury monoxide: A systematic investigation of its ground electronic state. *The Journal of Physical Chemistry A*, *107*(26), 1783–1787. https://doi.org/10.1002/chin.200326001

Si, L., & Ariya, P. A. (2008). Reduction of oxidized mercury species by dicarboxylic acids (C2-C4): Kinetic and product studies. *Environmental Science & Technology*, *42*(14), 5150–5155. https://doi.org/10.1021/es800552z

Sigler, J. M., Mao, H., & Talbot, R. (2009). Gaseous elemental and reactive mercury in Southern New Hampshire. *Atmospheric Chemistry and Physics*, *9*(6), 1929–1942. https://doi.org/10.5194/acp-9-1929-2009

Sillman, S., Marsik, F. J., Al-Wali, K. I., Keeler, G. J., & Landis, M. S. (2007). Reactive mercury in the troposphere: Model formation and results for Florida, the northeastern United States, and the Atlantic Ocean. *Journal of Geophysical Research*, *112*(D23). https://doi.org/10.1029/2006jd008227

Skamarock, W. C., Klemp, J. B., Dudhia, J., Gill, D. O., Barker, D. M., Duda, M. G., et al. (2008). A description of the advanced research WRF version 3. https://doi.org/10.5065/D68S4MVH

Stull, D. R. (1947). Vapor pressure of pure substances. Organic and inorganic compounds. *Industrial & Engineering Chemistry*, *39*(4), 517–540. https://doi.org/10.1021/ie50448a022

Subir, M., Ariya, P. A., & Dastoor, A. P. (2011). A review of uncertainties in atmospheric modeling of mercury chemistry I. Uncertainties in existing kinetic parameters - Fundamental limitations and the importance of heterogeneous chemistry. *Atmospheric Environment*, *45*(32), 5664–5676. https://doi.org/10.1016/j.atmosenv.2011.04.046

Tossell, J. A. (2003). Calculation of the energetics for oxidation of gas-phase elemental Hg by Br and BrO [Article]. *Journal of Physical Chemistry A*, *107*(39), 7804–7808. https://doi.org/10.1021/jp030390m

Wu, L. (2024). Improving simulation of gas-particle partitioning of atmospheric mercury using CMAQ-newHg-Br v2 [Model]. Zenodo. https://doi.org/10.5281/zenodo.10698554

Wu, R., Castro, P. J., Gaito, C., Beiter, K., Dibble, T. S., & Wang, C. (2022). Combined experimental and computational kinetics studies for the atmospherically important BrHg radical reacting with NO and O(2). *The Journal of Physical Chemistry A*, *126*(24), 3914–3925. https://doi.org/10.1021/acs.jpca.2c02531

Wu, R., Wang, C., & Dibble, T. S. (2020). First experimental kinetic study of the atmospherically important reaction of BrHg + NO2. *Chemical Physics Letters*, *759*, 137928. https://doi.org/10.1016/j.cplett.2020.137928

Yahya, K., Wang, K., Campbell, P., Glotfelty, T., He, J., & Zhang, Y. (2016). Decadal evaluation of regional climate, air quality, and their interactions over the continental US and their interactions using WRF/Chem version 3.6.1. *Geoscientific Model Development*, *9*(2), 671–695. https://doi.org/10.5194/gmd-9-671-2016

Yarwood, G., Jung, J., Whitten, G. Z., Heo, G., Mellberg, J., & Estes, M. (2010). *Updates to the Carbon bond Mechanism for version 6 (CB6) the 9th annual CMAS conference*. Chapel Hill.

Ye, Z. Y., Mao, H. T., Driscoll, C. T., Wang, Y., Zhang, Y. X., & Jaegle, L. (2018). Evaluation of CMAQ coupled with a state-of-the-art mercury chemical mechanism (CMAQ-newHg-Br) [Article]. *Journal of Advances in Modeling Earth Systems*, *10*(3), 668–690. https://doi.org/10.1002/2017ms001161

Zhang, H., Holmes, C. D., & Wu, S. (2016). Impacts of changes in climate, land use and land cover on atmospheric mercury. *Atmospheric Environment*, *141*, 230–244. https://doi.org/10.1016/j.atmosenv.2016.06.056

Zhang, H., Wang, Z. W., Wang, C. J., & Zhang, X. S. (2019). Concentrations and gas-particle partitioning of atmospheric reactive mercury at an urban site in Beijing, China [Article]. *Environmental Pollution*, *249*, 13–23. https://doi.org/10.1016/j.envpol.2019.02.064

Zhang, L., Blanchard, P., Gay, D. A., Prestbo, E. M., Risch, M. R., Johnson, D., et al. (2012). Estimation of speciated and total mercury dry deposition at monitoring locations in eastern and central North America. *Atmospheric Chemistry and Physics*, *12*(9), 4327–4340. https://doi.org/10.5194/acp-12-4327-2012

Zhang, L., Wright, L. P., & Blanchard, P. (2009). A review of current knowledge concerning dry deposition of atmospheric mercury. *Atmospheric Environment*, *43*(37), 5853–5864. https://doi.org/10.1016/j.atmosenv.2009.08.019

Zhang, L., Wu, Z., Cheng, I., Wright, L. P., Olson, M. L., Gay, D. A., et al. (2016). The estimated six-year mercury dry deposition across North America. *Environmental Science & Technology*, *50*(23), 12864–12873. https://doi.org/10.1021/acs.est.6b04276

Zhang, P., & Zhang, Y. (2022). Earth system modeling of mercury using CESM2 – Part 1: Atmospheric model CAM6-Chem/Hg v1.0. *Geoscientific Model Development*, *15*(9), 3587–3601. https://doi.org/10.5194/gmd-15-3587-2022

Zhang, Y., Jaegle, L., van Donkelaar, A., Martin, R. V., Holmes, C. D., Amos, H. M., et al. (2012). Nested-grid simulation of mercury over North America. *Atmospheric Chemistry and Physics*, *12*(14), 6095–6111. https://doi.org/10.5194/acp-12-6095-2012

References From the Supporting Information

Ariya, P. A., Khalizov, A., & Gidas, A. (2002). Reactions of gaseous mercury with atomic and molecular halogens: Kinetics, product studies, and atmospheric implications. *Journal of Physical Chemistry A*, *106*(32), 7310–7320. https://doi.org/10.1021/jp020719o

Balabanov, N. B., Shepler, B. C., & Peterson, K. A. (2005). Accurate global potential energy surface and reaction dynamics for the ground state of HgBr2 [Article]. *Journal of Physical Chemistry A*, *109*(39), 8765–8773. https://doi.org/10.1021/jp053415l

Burkholder, J. B., Sander, S. P., Abbatt, J. P. D., Barker, J. R., Cappa, C., Crounse, J. D., et al. (2020). Chemical kinetics and photochemical data for use in atmospheric studies.

Donohoue, D. L., Bauer, D., Cossairt, B., & Hynes, A. J. (2006). Temperature and pressure dependent rate coefficients for the reaction of Hg with Br and the reaction of Br with Br: A pulsed laser photolysis-pulsed laser induced fluorescence study. *The Journal of Physical Chemistry A*, *110*(21), 6623–6632. https://doi.org/10.1021/jp054688j

Frances-Monerris, A., Carmona-Garcia, J., Acuna, A. U., Davalos, J. Z., Cuevas, C. A., Kinnison, D. E., et al. (2020). Photodissociation mechanisms of major mercury(II) species in the atmospheric chemical cycle of mercury. *Angewandte Chemie International Edition*, *59*(19), 7605–7610. https://doi.org/10.1002/anie.201915656

Pal, B., & Ariya, P. A. (2004). Gas-phase HO•-Initiated reactions of elemental mercury: Kinetics, product studies, and atmospheric implications. *Environmental Science & Technology*, *38*(21), 5555–5566. https://doi.org/10.1021/es0494353

Pankow, J. F. (1987). Review and comparative-analysis of the theories on partitioning between the gas and aerosol particulate phases in the atmosphere [Review]. *Atmospheric Environment*, *21*(11), 2275–2283. https://doi.org/10.1016/0004-6981(87)90363-5

Pleim, J., & Ran, L. (2011). Surface flux modeling for air quality applications. *Atmosphere*, *2*(3), 271–302. https://doi.org/10.3390/atmos2030271

Tokos, J. J. S., Hall, B. O., Calhoun, J. A., & Prestbo, E. M. (1998). Homogeneous gas-phase reaction of Hg° with H_2O_2, O3, CH3I, AND (CH3) 2S: Implications for atmospheric Hg cycling. *Atmospheric Environment*, *32*(5), 823–827. https://doi.org/10.1016/S1352-2310(97)00171-4

Wang, F., Saiz-Lopez, A., Mahajan, A. S., Gómez Martín, J. C., Armstrong, D., Lemes, M., et al. (2014). Enhanced production of oxidised mercury over the tropical Pacific Ocean: A key missing oxidation pathway. *Atmospheric Chemistry and Physics*, *14*(3), 1323–1335. https://doi.org/10.5194/acp-14-1323-2014

Wilcox, J. (2009). A kinetic investigation of high-temperature mercury oxidation by chlorine [Article]. *Journal of Physical Chemistry A*, *113*(24), 6633–6639. https://doi.org/10.1021/jp901050d